

Alloy Shrinkage Factors for the Investment Casting Process

ADRIAN S. SABAU

This study deals with the experimental measurements and numerical predictions of alloy shrinkage factors (SFs) related to the investment casting process. The dimensions of the A356 aluminum alloy casting were determined from the numerical simulation results of solidification, heat transfer, fluid dynamics, and deformation phenomena. The investment casting process was carried out using wax patterns of unfilled wax and shell molds that were made of fused silica with a zircon prime coat. The dimensions of the die tooling, wax pattern, and casting were measured, in order to determine the actual tooling allowances. Several numerical simulations were carried out, to assess the level of accuracy for the casting shrinkage. The solid fraction threshold, at which the transition from the fluid dynamics to the solid dynamics occurs, was found to be important in predicting shrinkage factors (SFs). It was found that accurate predictions were obtained for all measured dimensions when the shell mold was considered a deformable material.

I. INTRODUCTION

DETERMINATION of the pattern-tooling dimensions is the first and most important step in the investment casting process; it is critical for obtaining cast parts with accurate dimensions. The dies for investment are prepared in three steps. First, wax patterns are prepared by injecting wax into previously prepared dies. Second, ceramic shells are made by the successive application of ceramic coatings over the wax patterns. Finally, the alloys are cast into the dewaxed shell molds. The dimensional changes associated with either the wax, the shell mold, or the alloy are referred to as wax, shell mold, or alloy shrinkage factors (SFs) (or tooling allowances), respectively. It is the typical practice to calculate the dimensions of the die tools by adjusting the nominal casting dimensions by the SFs. At the end of the casting process, the nominal casting dimensions can be achieved if the die tools were dimensioned with the appropriate degree of accuracy.

Rosenthal^[1] indicated that metal shrinkage during casting is one of the largest components of the overall dimensional changes between the pattern tooling and the part. For parts that have only unrestricted dimensions (*i.e.*, parts in which neither die pieces nor cores restrict the shrinkage of the part), predictions of the final part of the dimensions based solely on their thermal expansion property are appropriate. However, most of the parts fabricated in the investment casting process are very complex and have constrained dimensions. For constrained dimensions, investment casting engineers adjust the unconstrained shrinkage allowances based on their experience and on trial and error.

The critical properties of the alloy materials that have to be considered for calculating casting dimensions were reviewed by Sabau and Viswanathan.^[2] They concluded that the solidification, heat transfer, stress state, and ensuing deformation behavior of the metal in the semisolid and solid state must be considered, in order to predict the final dimen-

sions in the investment casting process. For permanent mold castings, Bellet *et al.*^[3] found that the combined effect of thermoelastic, plastic, and creep-induced strain-stress fields must be considered, in order to predict the final shape. The stresses generated during casting solidification has been a topic of many studies, including those by Drezet and Rappaz;^[4] Schwerdtfeger *et al.*;^[5] and Dahle *et al.*^[6] Miller^[8] used the model introduced by Kim *et al.*^[9] to study the deformation of aluminum alloy parts during the diecasting process, while Sabau and Viswanathan^[2] reviewed constitutive equations for alloy deformation.

The effects of shell properties on alloy deformation were discussed in more detail by Snow.^[10] Piwonka^[11] indicated that the deformation of the mold must be considered in order to predict the final dimensions of the investment casting parts. However, there are no results that illustrate the effect of shell mold deformation on the final dimensions of diecast parts.

The main goal of this study is to predict the alloy tooling allowances, based on a combined analysis of heat-transfer and deformation phenomena, for the A356 aluminum alloy. The wax patterns were invested at Minco, Inc. (Midway, TN), and casting experiments were conducted at Precision Metalsmiths, Inc. (PMI, Cleveland, OH), using the shell molds that were made of fused silica with a zircon prime coat. The properties of the shell molds made of fused silica with a zircon prime coat were provided in Sabau and Viswanathan.^[2] Sabau^[12] showed that accurate temperature predictions were obtained when heat-transfer coefficients (HTCs) at mold surfaces were based on natural convection correlations. Two visco-elastoplastic constitutive equations that were proposed by Bellet *et al.*^[3] and Kim *et al.*^[9] for aluminum alloys were used in this study.

II. THERMOPHYSICAL PROPERTY DATA

The first step in predicting alloy SFs was the determination of the thermophysical properties of the A356 aluminum alloy. Density measurements in a temperature range of 20 °C to 800 °C were carried out, using a push-rod dilatometer. The solid fraction distribution depends on the temperature and the cooling rate. The cooling rate was estimated from the cooling curves that were obtained for a similar mold and casting.^[12] The estimated cooling rate for the alloy was approximately

ADRIAN S. SABAU, Staff Member, is with the Metals and Ceramics Division, Oak Ridge National Laboratory, Oak Ridge, TN 37831-6083. Contact e-mail: sabaua@ornl.gov

Manuscript submitted April 11, 2005.

Table I. Volumetric Solid Fraction, g_s , Volumetric Fraction of Eutectic Solid Phase, g_E , Liquid Phase Density, ρ_l , Solid Phase Density, ρ_s , and Average Phase Density, ρ_0 , for A356 Aluminum Alloy

T (°C)	g_s	g_E	ρ_l (g/cm ³)	ρ_s (g/cm ³)	ρ_0 (g/cm ³)
20.37	—	—	—	—	2.670
545.0	1.00	0.530	2.58	2.45	2.562
554.0	0.970	0.500	2.58	2.45	2.560
559.0	0.950	0.480	2.58	2.45	2.558
561.0	0.930	0.460	2.58	2.45	2.555
568.0	0.890	0.420	2.58	2.45	2.550
572.0	0.850	0.380	2.58	2.45	2.545
575.0	0.780	0.310	2.58	2.45	2.536
577.0	0.730	0.260	2.58	2.45	2.529
579.0	0.470	0.00	2.54	2.45	2.495
594.7	0.360	0.00	2.54	2.44	2.476
606.7	0.250	0.00	2.54	2.43	2.456
618.7	0.0630	0.00	2.54	2.42	2.424
620.0	0.00	0.00	2.54	2.41	2.415
800.0	—	—	—	—	2.368

0.5 °C/s, or 30 °C/min. The alloy solidification was studied using a differential scanning calorimetry (DSC) instrument. The DSC measurements were conducted at cooling rates of 20 °C/min. The distribution of the solid fraction was determined by post-processing the original DSC data,^[13,14] using a desmearing procedure similar to those by Dong and Hunt^[15] and Boettinger and Kattner.^[16] Thus, instead of simply integrating the DSC signal, a more accurate distribution of the solid fraction was obtained. The thermophysical properties of A356 aluminum alloy are shown in Table I.

The thermal conductivity of the liquid phase and the specific heat of the A356 aluminum alloy were measured as 90 W/m/K and 1.17 J/g/K, respectively. The latent heat was determined by DSC to be 456 J/g. The density variation with temperature was used to estimate the thermal expansion property that was needed for the thermomechanical model.

III. THERMOMECHANICAL ALLOY DEFORMATION

Several advanced models for the numerical simulation of stress, strain, and the ensuing displacement fields during casting have been developed in academia over the last decade.^[3,4] These models were recently implemented in the commercial simulation software ProCAST.* The stress module

*ProCAST is a trademark of ESI Group, France.

was coupled with the fluid-flow module in ProCAST, such that appropriate constitutive equations were available for the liquid, semisolid, and solid states that coexist during casting solidification. Depending on the amount of solid fraction, the deformation or fluid-flow phenomena takes place as shown in Table II, where f_s is the mass solid fraction, f_{ch} is the mass solid fraction at the coherency point, and f_{pk} is the mass solid fraction at the maximum packing point. The maximum packing point represents the instant at which the solid particles interlock with each other, providing rigidity.^[7] The solid fractions critical to the thermomechanical behavior of the A356 aluminum alloy during alloy solidification

Table II. Fluid-Flow and Deformation Mechanisms Depending on the Solidifying Microstructure^[7]

Solidification Domain	Microstructure	Fluid Flow	Deformation
$f_s < f_{ch}$	floating equiaxed crystals	mass feeding	not applicable (i.e., no yield strength)
$f_{ch} < f_s < f_{pk}$	dendritic network gets established; packing increases	mass feeding reduces; interdendritic feeding increases	low-yield point increases slowly (0 to 0.01 MPa)
$f_{pk} < f_s$	dendritic network	interdendritic feeding	yield point increases faster (0.01 to 0.9 MPa)

Table III. Critical Solid-Mass Fractions for A356 Aluminum Alloy^[17]

Solidification Characteristics	Temperature (°C)	Solid Fraction (pct)
Liquidus	610 to 617	0
Dendrite coherency	598 to 604	19 to 29
Eutectic	565 to 570	51 to 56
Rigidity point	565 to 567	63 to 74
Solidus	540 to 533	1

were determined from experimental data obtained by Arnberg *et al.*^[17] (Table III).

According to the small-strain theory, the total strain can be decomposed into strain components that correspond to the elastic, viscoplastic, thermal, and liquid-solid phase-transformation effects. The elastic strain was related to the internal stresses, by Hook's law. Bellet *et al.*^[3] developed a methodology for modeling the casting solidification by including constitutive equations for the mushy zone and liquid regions in a solid model that is based on Perzyna's work.^[18] A Norton–Hoff power law to describe the viscoplastic behavior of an Al-7Si-0.3Mg alloy^[3] is as follows:

$$\dot{\epsilon}^{pl} = \gamma \left\langle \frac{\sigma_{eq}}{\sigma_0} - 1 \right\rangle^{1/m}, \quad \gamma = \frac{1}{\sqrt{3}} \left(\frac{\sigma_0}{\sqrt{3}K} \right)^{\frac{1}{m}} \quad [1]$$

where $\dot{\epsilon}^{pl}$ = the plastic strain rate; the operator $\langle \cdot \rangle$ is defined as $\langle f \rangle = f$ when $f \geq 0$ and zero otherwise; γ = the fluidity of the material; m = the strain rate sensitivity coefficient; K = the viscoplastic consistency; σ_0 = the yield stress; and σ_{eq} = the von Mises equivalent stress.

Both γ and m were temperature-dependent coefficients. For example, at low temperatures, when the alloy tends to behave elastoplastically, m has very small values, while γ has very large values. In ProCAST,^[19] the power exponent n and a viscous parameter η are used instead of the variables m and γ , respectively. The following relationships provide a connection between the variables used by Bellet *et al.*^[3] and those in ProCAST (Table IV):

$$n = 1/m \quad \text{and} \quad \eta = 1/\sqrt{1.5} \quad [2]$$

Table IV. Mechanical Properties Used in ProCAST Based on Bellet *et al.*^[3]

Temperature (°C)	E (MPa)	σ_0 (MPa)	ν	n	η (s)
25	60,000	200	0.33	50	0
100	—	—	—	21.3	8.320×10^{-17}
200	—	—	—	12.4	5.000×10^{-10}
300	—	—	—	8.75	3.040×10^{-7}
400	—	—	—	6.76	1.000×10^{-5}
545	34,000	1	0.33	5	1.656×10^{-4}
572	34,000	1	0.33	5	—
573	0.01	0.01	0.49	0.2	—
579	—	—	—	0.2	—
600	—	—	—	1	—
615	0.01	0.01	0.49	1	1.656×10^{-4}

Table V. Mechanical Properties Used in ProCAST, Based on Kim *et al.*^[9]

Temperature (°C)	E (MPa)	σ_0 (MPa)	H (MPa)
20	71,705	186	7170
200	69,636	172	6963
300	63,776	116	6377
400	57,226	54	5722
500	36,542	31	3654
550	6894	—	689
556	1434	9	143
616	143	1	14

ProCAST allows modeling of the liquid regions by the Navier–Stokes equations, eliminating the need to artificially extend the stress model to liquid regions. Kim *et al.*^[9] proposed an elastoplastic model based on the linear hardening model (Table V), which is now a part of the stress database in ProCAST. According to this model, the linear hardening law is defined as

$$\sigma_Y = \sigma_0 + H\varepsilon^{pl} \quad [3]$$

where σ_0 = the yield stress; ε^{pl} = the plastic strain; H = the plastic modulus; and σ_Y = the modified yield stress due to linear hardening. The viscoplastic behavior is described by the following equation:

$$\dot{\varepsilon}^{pl} = \frac{1}{\eta} \langle |\sigma| - \sigma_Y \rangle^n \frac{\sigma}{|\sigma|} \quad [4]$$

where σ is the applied stress. A linear temperature variation between consecutive data points was assumed to calculate the variables shown in Tables IV and V.

IV. EXPERIMENTAL RESULTS

The parts with six steps were examined in this study (Figure 1). The 2.54-cm-thick step is considered to be step 1. Two types of stepped parts were made: parts without holes and parts with holes, on steps 3 and 5. In the remainder of this study, the alloy castings and wax patterns are simply referred to as parts and patterns. The patterns without holes and patterns with two holes are referred to as no-hole, or unre-

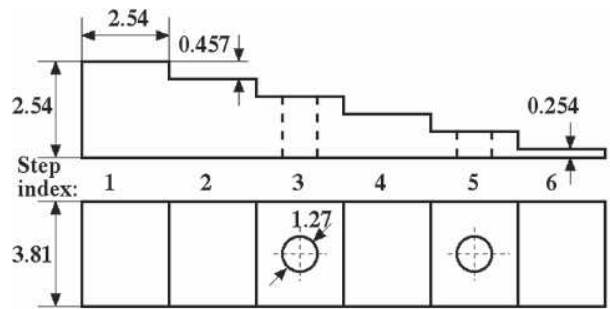


Fig. 1—Wax pattern dimensions (cm) and step index.

strained, patterns and two-hole, or restrained, patterns, respectively. The two-hole patterns were made by placing cores in the die. The two cores provided geometrical restraint on the length dimension of the part. For this work, wax patterns were made at M. Argueso & Co. (Muskegon, MI), by injection of liquid unfilled wax, CERITA* 29-51 at a pressure of

*CERITA is a trademark of M. Argueso & Co.

1.7 MPa (250 psi), at 65 °C, with a dwell time of 120 seconds.

The casting configuration used in this study consisted of a downsprue, a runner, and one casting (Figure 2). The sprue was dimensioned such that there was enough metallostatic head to fill the entire part. The heights of the downsprue and pouring cup were 17 and 6.35 cm, respectively. The horizontal cross-section dimensions were 6.35×6.35 , 2.54×2.54 , and 2.54×1.9 cm at the top and the end of the pouring cup and at the end of the sprue, respectively.

The shell mold contained the following types of substrates: face coats, intermediate coats, backup coats, and seal coats. Each coat was generally made of two layers: a slurry layer and a stucco layer. In this study, zircon and fused-silica shell materials were used (Table VI). The shell mold had eight coats: a zircon prime coat, one intermediate coat, five backup coats, and one dip coat. The shell mold thickness was approximately 8.5 mm. The molds were preheated in two furnaces. The first furnace was used for sintering the molds at temperatures of 1000 °C. After sintering, the shell molds were placed in the second furnace and held at 400 °C, in order to insure a uniform temperature distribution in the molds.

The dimensions of the die tool, the wax patterns, and the casting were measured at the same locations, using a coordinate measurement machine (CMM). The CMMs are widely used throughout manufacturing industries to meet high-quality standards and achieve dimensional accuracy. The probe size of the CMM was 3 mm in diameter. The probe tips were round to within 0.0005 mm, and the diameters were within 0.003 mm of the nominal diameter. The actual diameter of the probe tip was calibrated against a reference sphere with a roundness uncertainty of plus or minus 0.0001 mm and a diameter uncertainty of 0.0002 mm. The measurement precision was plus or minus 0.02 mm.

The dimensions of the wax pattern were measured, to provide a base line for the casting dimensions. The wax patterns were examined under magnification, to insure that no deformation was present in the surfaces after probing. The

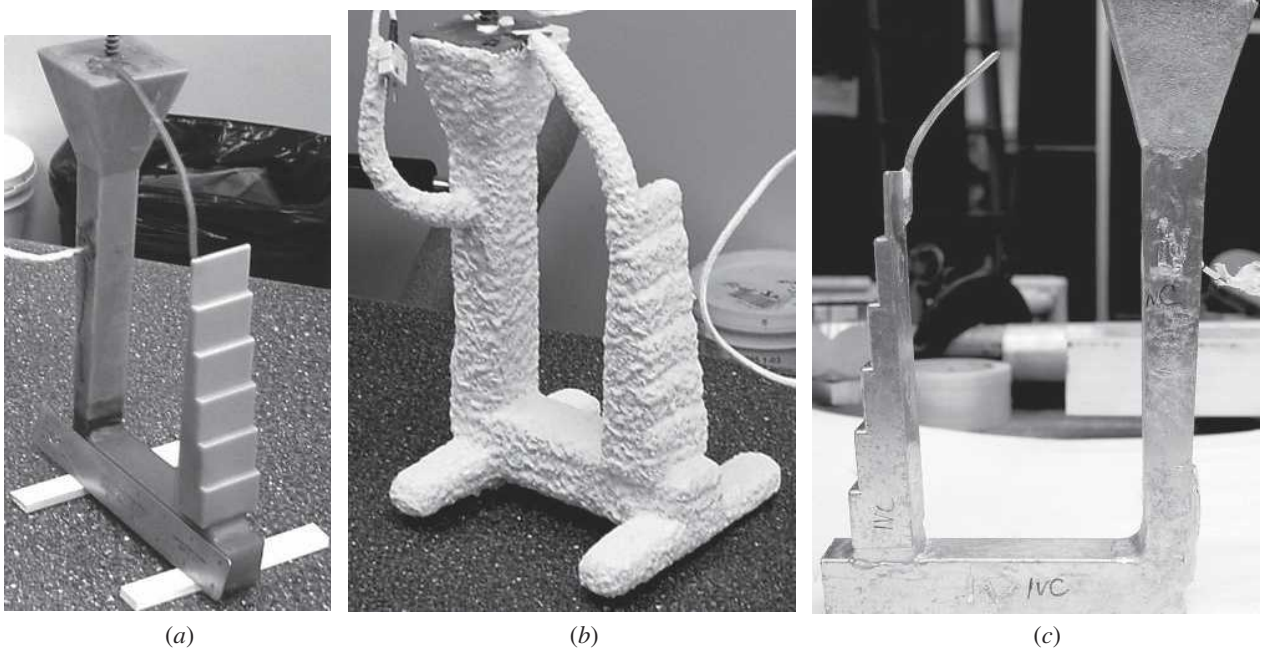


Fig. 2—Shell molds were invested at Minco, Inc., and casting experiments were conducted at PMI, Inc.: (a) wax pattern, (b) shell mold, and (c) aluminum casting.

Table VI. Shell Materials Selected for This Study (The Slurry Was Colloidal Silica, for All Coats)

Shell Coat	Stucco Material	Stucco Size	Flour Material	Flour Size
Face	zircon	GFN 110	zircon	50 pct 200 mesh and 50 pct 325 mesh
Intermediate	fused silica	-50 + 100 mesh	fused silica	120 mesh
Backup	fused silica	-30 + 50 mesh	fused silica	120 mesh
Seal	—	—	fused silica	120 mesh

position of the CMM measurement points are shown in Figure 3. The width shrinkage was calculated from the width coordinates for each pair of points, which were located at the same length and height, but were situated at opposite sides of the pattern. A representative length dimension was chosen to be L2-5, between the ends of steps 2 and 5. Four no-hole patterns and four two-hole patterns were injected. Since the wax pattern showed good reproducibility, only two castings were made for each case. The parts were labeled as shown in Table VII.

The dimensional variations were calculated using the following relationships:

$$\begin{aligned} \text{wax shrinkage } (w_s) &= \text{pattern dimensions} \\ &\quad - \text{die dimensions wax pattern} \\ \text{alloy shrinkage } (a_s) &= \text{casting dimensions} \\ &\quad - \text{pattern dimensions} \\ \text{casting shrinkage } (c_s) &= \text{pattern dimensions} \\ &\quad - \text{casting dimensions} \end{aligned}$$

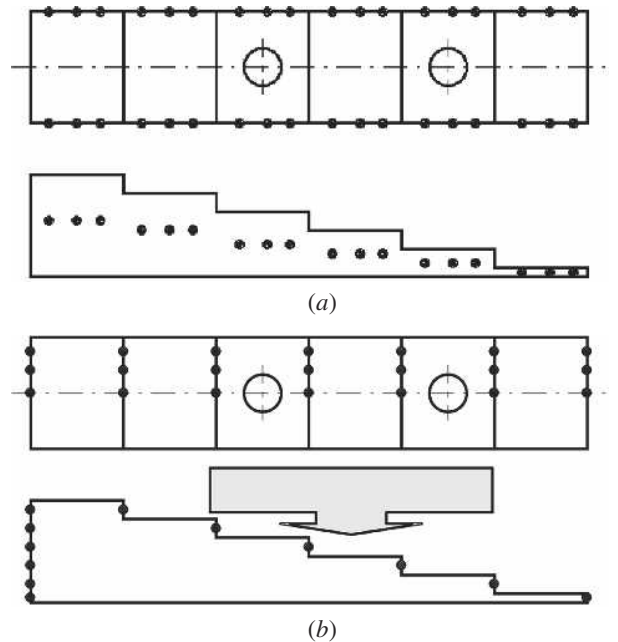
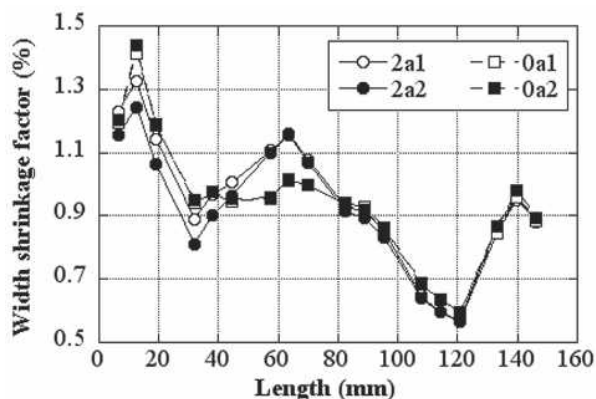


Fig. 3—The position of coordinate measurement points for (a) the width dimensions and (b) length L2-5, between ends of steps 2 and 5.

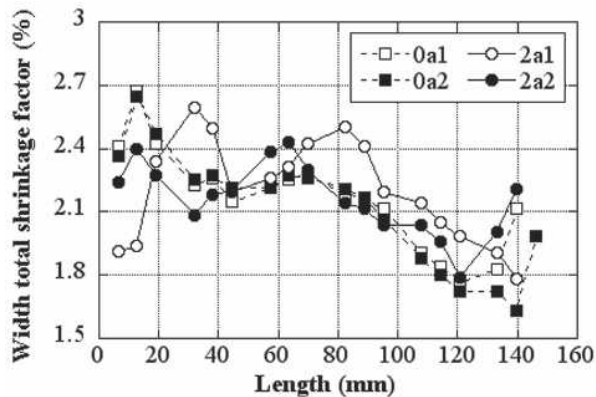
The shrinkage of L2-5 was calculated by subtracting the length coordinate of the points on step 5 from that of the corresponding points on step 2. The percentage of the shrinkage was calculated for all examined dimensional variations and the results are shown in Figures 4 and 5: the width shrinkage was nonlinear along the pattern length, in all cases. There was a high degree of reproducibility for

Table VII. Index of Wax Patterns and Castings

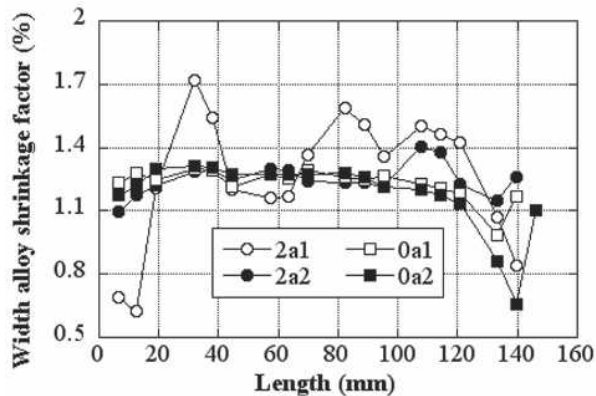
Part Index	Number of Holes in Part	Part Number
0a1	—	1
0a2	—	2
2a1	2	1
2a2	2	2



(a)



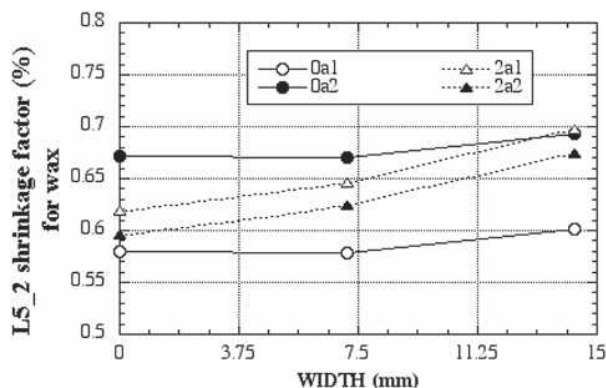
(b)



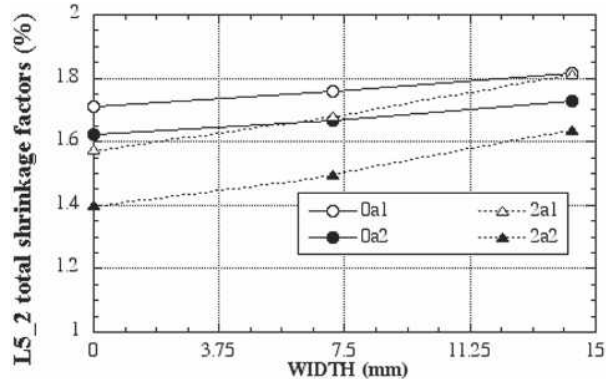
(c)

Fig. 4—Width-dimension SFs: (a) w_s , (b) c_s , and (c) a_s .

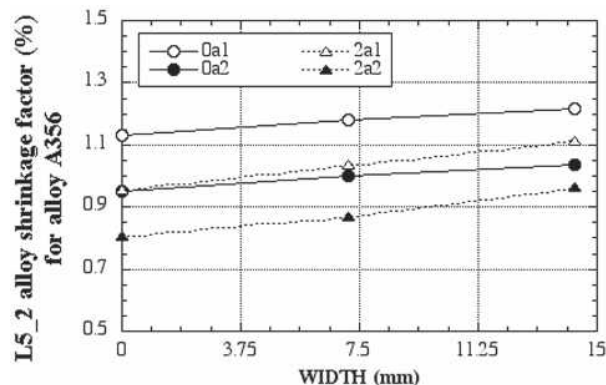
the wax patterns. The only difference in wax shrinkage between the dimensions of the unrestrained pattern and the restrained pattern was observed at step 3, where the longer



(a)



(b)



(c)

Fig. 5—The SFs for the length dimension, L2-5: (a) w_s , (b) c_s , and (c) a_s .

hole was made for the restrained pattern. The lowest wax shrinkage was observed at step 5, where the smaller hole was made. This effect is likely to be due to the small thickness of the steps, which results in faster cooling in this region.

For the L2-5 dimension, the shrinkage of the wax pattern had approximately the same values for both the restrained and unrestrained patterns, although the unrestrained pattern showed larger scatter in shrinkage. The points with a zero-width coordinate were located on the symmetry plane of the patterns, or centerline. The shrinkage

was minimal at the centerline and largest at the edges. A smaller length shrinkage was measured for the restrained pattern. As indicated in Figure 5(b), for the case of overall casting shrinkage, the unrestrained parts shrink more than the unrestrained ones. The same was observed for the alloy dimension, as well. The following general observations can be made concerning the dimensional measurements: (1) the width SFs were largest toward the more massive region of the casting (step 1) and decreases towards the thinner end (step 5); (2) the length SFs were larger at the edges than at the centerline; and (3) overall, the restrained pattern exhibited larger shrinkages, in both width-wise and lengthwise directions.

V. NUMERICAL SIMULATIONS RESULTS

Numerical simulations of the heat transfer, the solidification, and the deformation during casting, and the subsequent cooling, were conducted using ProCAST^[19] with the casting parameters, material properties, and boundary conditions that were given earlier in this article and in Sabau.^[12] The mesh was created using the shelling feature in MeshCAST,* a module of ProCAST (Figure 6).

*MeshCAST is a trademark of CoWave Networks, LosGates, CA.

One mesh layer of 0.66 mm (0.026 in.) was used for the zircon face coat and another layer of 0.9 mm (0.036 in.) was used for the intermediate fused-silica coat. Three layers, 1.2 mm (0.048 in.) each, were used to model the fused-silica backup coats. Shell molds were meshed and numerical simulations were carried out before the experiments were conducted. Since these simulation results indicated that the casting parts were free of shrinkage defects, the casting experiments proceeded as planned.

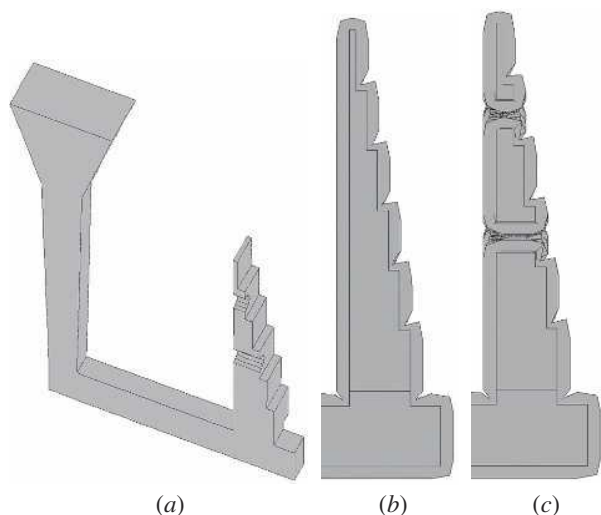


Fig. 6—Pictures of the casting configuration used for numerical simulations showing (a) the alloy material; (b) the shell mold around the casting without cores, having unrestrained deformation; and (c) the shell mold around the casting with cores, the length and width dimensions being partially constrained by cores.

In order to account for thermal radiation effects within the shell mold, the following relationship proposed by Sabau and Viswanathan in 2004,^[20] for the temperature dependence of thermal conductivity, k , was used:

$$k(T) = a_k + b_k T^3 \quad [5]$$

For a shell mold with a thickness of approximately 5 to 5.5 mm, coefficients a_k and b_k were found to be 0.85 and $6.25 \cdot 10^{-10}$, respectively.^[12] However, the average thickness of the shell molds, t_{sm} , used in this study was slightly higher, *i.e.*, 8.5 mm. Rather than creating new meshes, an additional numerical simulation was carried out to assess the effect of the larger mold thickness, where the thermal conductivity of the mold was decreased according to its thickness such that the insulating effect of a larger thickness would be properly accounted (*i.e.*, $t_{sm}/k = \text{constrained}$). The numerical simulation results showed that the effect of the shell-mold thickness on thermal conductivity was small (Table VIII) and thus, numerical simulation was performed using Eq. [5].

The HTC's for this study were determined using the methodology that was described in Reference 12, for the same combination of sprue and runner system as shown in Figure 2. In Reference 12, the two-plate mold was supported by firebricks, altering the airflow pattern of the natural convection around the mold. The casting configuration in this study was simplified by making only one part per casting and attaching the support structure directly to the wax pattern. The mold support was invested (Figure 2(a)), allowing a more uniform cooling around the stepped pattern. The HTC's for the mold-air interface around the part, sprue, and runner were determined to be 17, 38, and $7.5 \text{ W/m}^2 \text{ K}$, respectively, while the HTC's for the metal surface at the top sprue, the bottom surface of the mold in contact with the sand, and the metal-mold interface were determined to be 30, 42, and $850 \text{ W/m}^2 \text{ K}$, respectively.

Thermomechanical models developed by Bellet *et al.*^[3] and Kim *et al.*^[9] were used to study the effect of mold rigidity and alloy rigidity point on alloy SFs. The different cases considered for the numerical simulations are shown in Table IX. The packing point, f_{pk} , is considered to be the

Table VIII. Effect of Mold Thickness on Shrinkage of the L2-5 Dimension

Equivalent Mold Thickness (mm)	a_k	b_k	Unrestrained Shrinkage (Pct)	Restrained Shrinkage (Pct)
5.23	0.85	6.25×10^{-10}	1.84	1.1
8.5	0.48	3.61×10^{-10}	1.8	1

Table IX. Cases Considered in Numerical Simulations

Index Case No-Hole Part	Index Case Two-Hole Part	Thermomechanical Properties Reference	f_{pk} (Pct)	Shell Mold
1-0h	1-2h	Bellet*	90	rigid
2-0h	2-2h	Kim**	90	rigid
3-0h	3-2h	Kim**	70	rigid
4-0h	4-2h	Kim**	90	elastic
5-0h	5-2h	Kim**	70	elastic

*Bellet *et al.*^[2]

**Kim *et al.*^[7]

point at which the stress calculations started in ProCAST. For $f_S < f_{pk}$, liquid regions were taken into account, while for $f_S \geq f_{pk}$, the solid models were used in numerical simulation (Tables IV and V). When the shell mold was considered to be a linear-elastic material, the Young's modulus of 2586 MPa that was provided by Minco, Inc., was used for numerical simulation.^[21]

The numerical simulation results for the alloy shrinkage are shown in Figures 7 and 8, for the length and width dimensions, respectively. As shown in Figures 7(a) and (c) and 8(a) and (c), the results for the two thermomechanical models were close to each other for all the dimensions measured in the cases 1-0h, 2-0h, 1-2h, and 2-2h, irrespective of mold restraints. Thus, in the remainder of this study, the results were presented only for the Kim's model.

The measured dimensions were grouped according to the level of mold constraints. The unrestrained dimension groups include the length L2-5 for the no-hole pattern, and the width, W , for the no-hole pattern and two-hole pattern. The length L2-5 for the two-hole pattern was restrained by the shell mold. For a rigid mold and $f_{pk} = 90$ pct, the SFs were well predicted for the unrestrained dimensions but underpredicted for the restrained dimensions (cases 2-0h and 2-2h).

In an attempt to obtain higher shrinkage, the f_{pk} was lowered to 70 pct and cases 3-0h and 3-2h were simulated. As

f_{pk} was lowered to 70 pct, the model allowed for an increased deformation of the alloy in the mushy zone, due to the thermal expansion behavior and low stiffness. For a rigid mold and $f_{pk} = 70$ pct, the SFs were overpredicted in the case of the unrestrained dimensions and underpredicted for the restrained dimensions. The fact that the SFs for the unrestrained dimensions were overpredicted indicated that unrealistic deformations were introduced in the model.

For an elastic mold and $f_{pk} = 90$ pct, the SFs were well predicted for both the unrestrained dimensions and restrained dimensions (cases 4-0h and 4-2h). In the case of $f_{pk} = 70$ pct (cases 5-0h and 5-2h), the SFs assuming elastic mold were overpredicted for the unrestrained dimensions; these were results that were consistent with those for the rigid-mold case (cases 3-0h and 3-2h). A comparison of the results of the experimental and numerical simulations indicates that the best results were obtained for the fourth case, in which an elastic mold and $f_{pk} = 90$ pct were considered (Table X).

Apart from SFs, the casting distortion and the state of residual stress was obtained from the numerical simulation results. Information on casting distortion can be used by engineers to visualize the extent of deformation, which is shown in more abstract terms by the SFs. The deformation results were obtained at the instant at which the temperature dropped below 100 °C. The temperature profile (Figure 9)

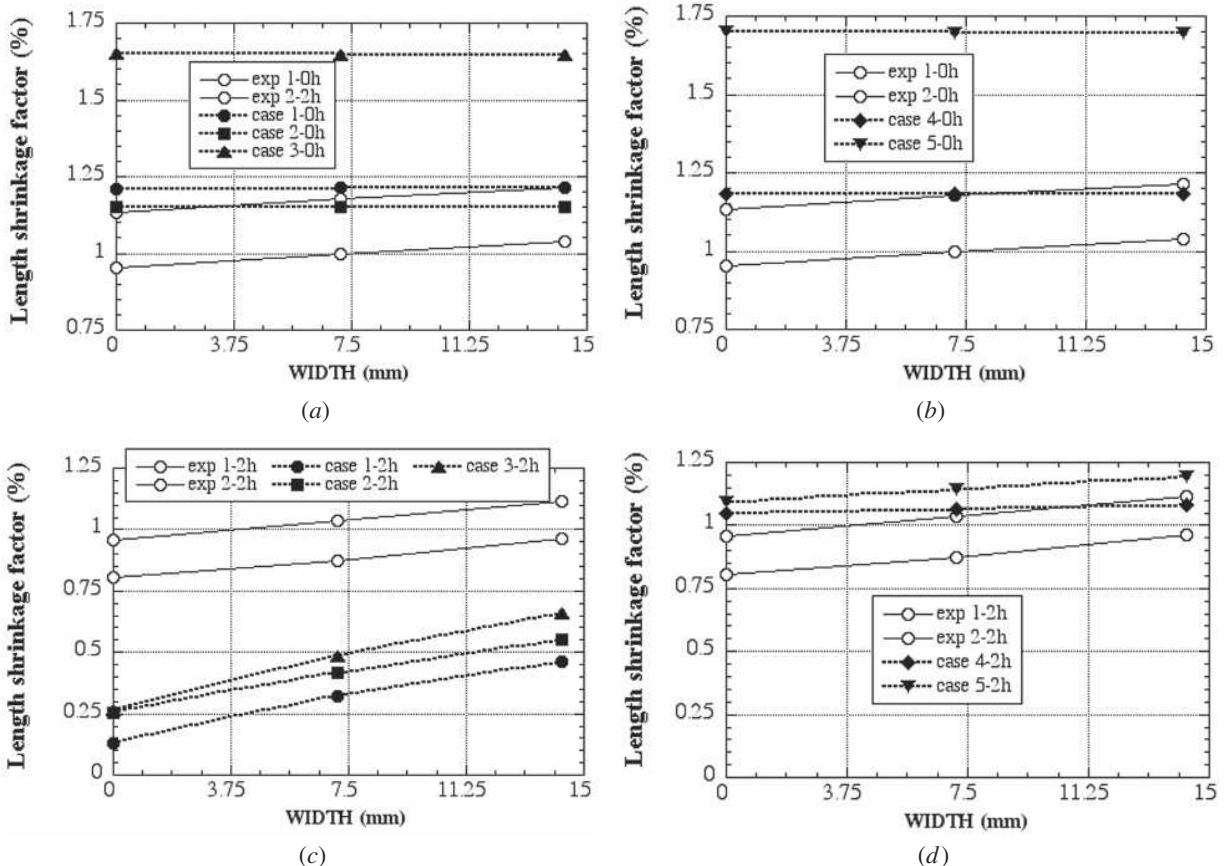


Fig. 7—The comparison between the experimental results and the computed results, for the length dimension, L2-5: (a) and (b) the part with no holes and (c) and (d) the part with two holes.

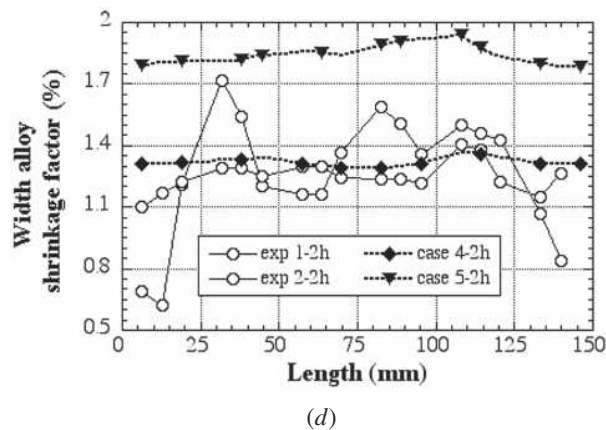
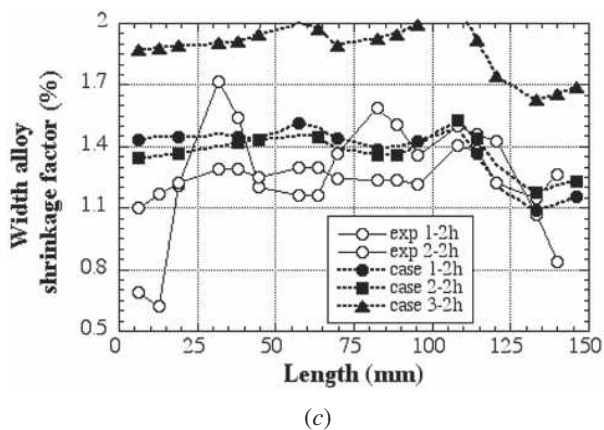
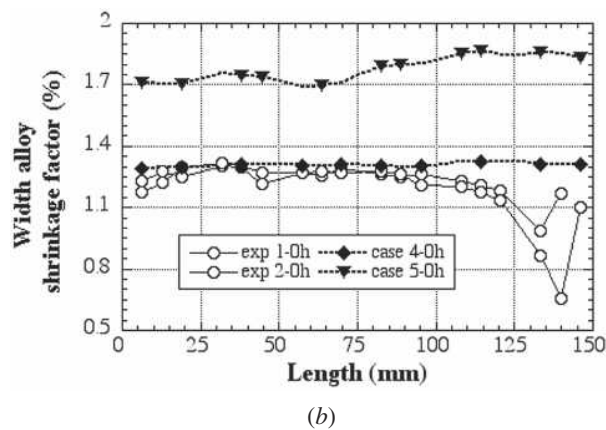
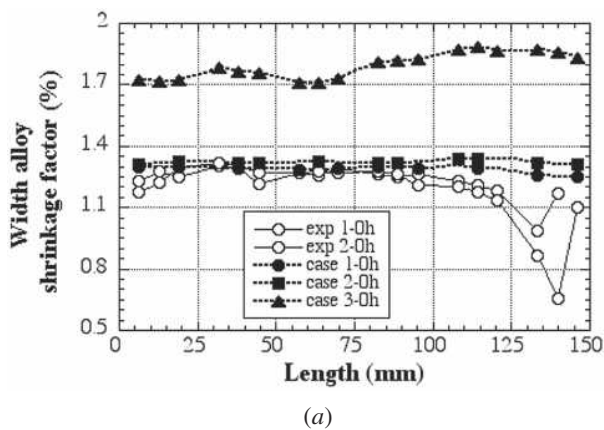


Fig. 8—The comparison between the experimental and the computed SFs for the width dimension as a function of length: (a) and (b) the part with no holes and (c) and (d) the part with two holes.

Table X. Summary of Numerical Simulation Results (– underpredicted, + overpredicted, X good agreement)

f_{pk} (pct)	Mold Type	Unrestrained Dimensions			Restrained Dimensions		Agreement
		L2-5 (No Holes)	W (No Holes)	W (Two Holes)	L2-5 (Two Holes)		
90	rigid	X	X	X	—		
70	rigid	+	+	+	—		
90	elastic	X	X	X	X	X	
70	elastic	+	+	+	X		

in the stepped part was found to be fairly uniform, varying from 90 °C to 100 °C.

In order to illustrate the effect of mold restraint, the contact-pressure distribution was shown in Figure 10. The pressure distribution that was calculated on the surface of the two holes indicates that the mold was under compression between the two holes. Since the elastic modulus of the mold was lower than that of the alloy, the mold provides limited resistance to the thermal contraction of the alloy. As shown by our results, this interaction between the alloy and mold, especially in partially restrained regions, is very important for predicting alloy SFs.

The distribution of the air gap and the distribution of the width displacement were shown in Figures 11 and 12, respec-

tively. The width displacement distribution shown in Figure 12 was half of the shrinkage for the width dimension. The magnitude of the width displacement indicates that the surface deformation was not uniform. Since the mold is elastic, the distributions of the air gap and the alloy displacement were not the same. This information can be used to identify surface sink defects, or to obtain better resolution for the SFs.

VI. SUMMARY AND CONCLUSIONS

The experimental and computational study of alloy SFs for the investment casting process were carried out for parts

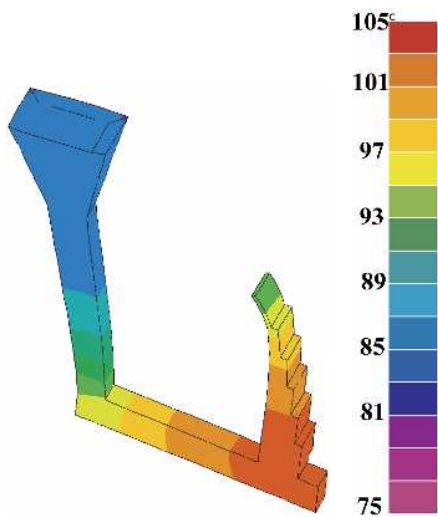


Fig. 9—Temperature profile in the alloy. Deformation was magnified 15 times.

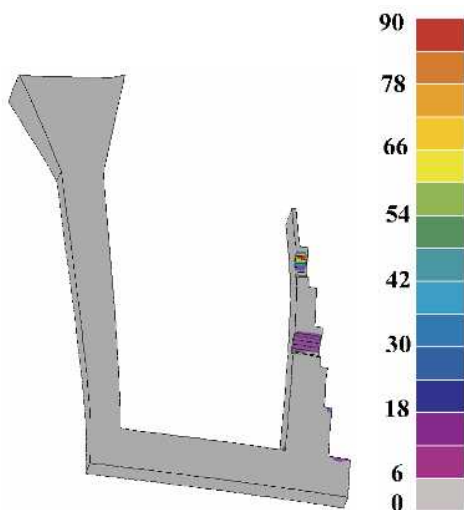


Fig. 10—Contact pressure due to mold restraint. Deformation was magnified 15 times

that have unrestrained dimensions and parts that have dimensions restrained by cores. The alloy deformations were predicted numerically by taking into account the thermo-mechanical properties of the alloy and the shell-mold materials. The measured dimensions were grouped according to the level of mold constraint. When the shell mold was considered to be a rigid body, the restrained dimensions were underpredicted, indicating that the rigidity of the ceramic mold was not high enough to prevent mold deformation. The solid-fraction threshold, at which the transition occurred from the fluid dynamics to the solid dynamics, was found to be an important factor for predicting SFs. For the thermomechanical models considered, the SFs were well predicted for both the unrestrained dimensions and the restrained dimensions, when the solid-fraction threshold was 90 pct. The results for the casting distortion were also included.

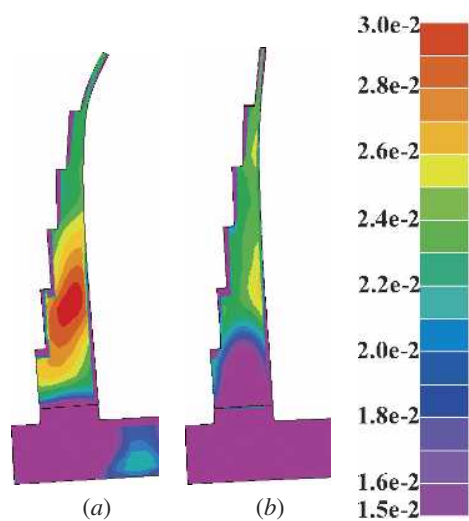


Fig. 11—Distribution of the air gap (cm) for (a) the no-hole casting and (b) the two-hole casting. Deformation was magnified 15 times.

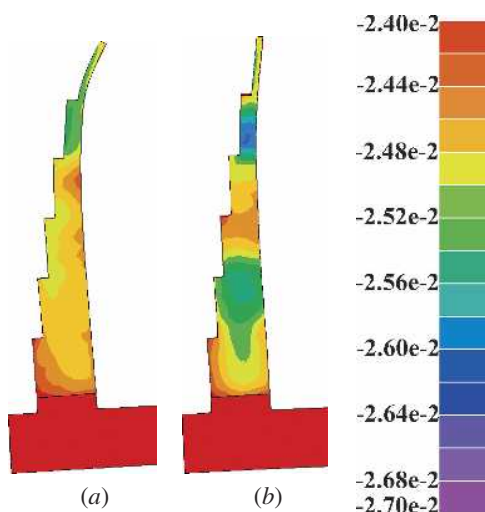


Fig. 12—Displacement distribution (cm) for (a) the no-hole casting and (b) the two-hole casting. Deformation was magnified 15 times.

ACKNOWLEDGMENTS

This work was performed as part of the project on Predicting Pattern Tooling and Casting Dimensions for Investment Casting, conducted in collaboration with the 4L Investment Casting Committee of the American Foundry Society and the Cast Metals Coalition.

We thank T. Wolf and I. Al-Rabadi, M. Argueso & Co., Inc., for assistance with wax injection experiments; J. Snow, D. Scott, and B. Sneider, Minco, Inc., for shell investment; R.A. Parham for assistance with thermocouples; Z. Wu, a University of Tennessee graduate student, for obtaining the SFs from the measured dimensions; J. Kovatch and R. Abramczyk, Precision Metalsmiths, Inc., for conducting casting experiments at their foundry; B. Schrey, Schrey & Sons Mold Co., for providing the sprue tooling; Jim Gardner, J.E.M. Manufacturing, for the casting design and for providing wax

patterns for the sprue; S. Viswanathan, Sandia National Laboratories, with whom we collaborated on past project tasks; M. Radovic and A. Wereszczak, Oak Ridge National Laboratory, for their review of the article; and Millie Atchley, for her assistance in typing the article.

The research was sponsored by the United States Department of Energy, Assistant Secretary for Energy Efficiency and Renewable Energy, Office of Industrial Technologies, Metal Casting Industries of the Future Program, under Contract No. DE-AC05-00OR22725 with UT-Battelle, LLC.

REFERENCES

1. H.H. Rosenthal: *Proc. 27th Annual Meeting of the Investment Casting Institute*, Rosemont, IL, 1979.
2. A.S. Sabau and S. Viswanathan: *Trans. Am. Foundry Soc.*, 2001, vol. 109, pp. 1-18.
3. M. Bellet, F. Decultieux, M. Menai, F. Bay, C. Levailant, J.L. Chenot, P. Schmidt, and I.L. Svensso: *Metall. Mater. Trans. B*, 1996, vol. 29B, pp. 81-99.
4. J.-M. Drezet and M. Rappaz: *Metall. Mater. Trans. A*, 1996, vol. 27A, pp. 3214-25.
5. K. Schwerdtfeger, M. Sato, and K.-H. Tacke: *Metall. Mater. Trans. B*, 1998, vol. 29B, pp. 1057-68.
6. A.K. Dahle, S. Instone, and T. Sumitomo: *Metall. Mater. Trans. A*, 2003, vol. 34A, pp. 105-13.
7. A.K. Dahle and D.H. StJohn: *Acta Mater.*, 1999, vol. 47, pp. 31-41.
8. A.R. Miller: *Prediction of Part Distortion in Die Casting*, Department of Energy Report for Project DE-FC07-97ID13577, The Ohio State University, Columbus, OH, 2002.
9. K.Y. Kim, H. Sakuta, and T. Suzuki: in *Modeling of Casting, Welding and Advanced Solidification Processes V*, M. Rappaz, K. Mahan, and M. Ozgu, eds., TMS, Warrendale, PA, 1991.
10. J.D. Snow: *Proc. 43rd Annual Meeting of the Investment Casting Institute*, Dallas, TX, Oct. 29–Nov. 1, 1995.
11. T.S. Piwonka: *8th World Conf. on Investment Casting*, London, 1993.
12. A.S. Sabau: *Trans. Am. Foundry Soc.*, 2005, vol. 113.
13. A.S. Sabau and W.D. Porter: unpublished research, 2005.
14. A.S. Sabau and W. Porter, *Analytical Models for System Errors of Differential Scanning Calorimetry Instruments*, ASME Heat Transfer/Fluids Engineering Summer Conf., Charlotte, NC, July 11–18, 2004.
15. H.B. Dong and J.D. Hunt: *J. Thermal Analysis and Calorimetry*, 2001, vol. 64, pp. 167-76.
16. W.J. Boettinger and U.R. Kattner: *Metall. Mater. Trans. A*, 2002, vol. 33A, pp. 1779-94.
17. L. Arnberg, L. Backerud, and G. Cahi: *Solidification Characteristics of Aluminum Alloys, Volume 3: Dendrite Coherency*, Des Plaines, IL, 1996.
18. P. Perzyna: *Q. Appl. Mathematics*, 1963, vol. 20, pp. 321-32.
19. D.M. Waite and M.T. Samonds: *Proc. 38th Annual Meeting of the Investment Casting Institute*, Dallas, TX, 1990.
20. A.S. Sabau and S. Viswanathan: *Trans. Am. Foundry Soc.*, 2004, vol. 112, pp. 649-61.
21. J.D. Snow, personal communication.